Stable Control of Force, Position, and Stiffness for Robot Joints Powered via Pneumatic Muscles

Barkan Ugurlu, *Member, IEEE*, Paolo Forni, Corinne Doppmann, Emre Sariyildiz, *Member, IEEE*, and Jun Morimoto, *Member, IEEE*

***Abstract*—This paper proposes a novel controller framework for antagonistically driven pneumatic artificial muscle (PAM) actuators. The proposed controller can be stably configured in both torque-stiffness control and position-stiffness control modes. Three contributions are sequentially presented in constructing the framework: 1) A PAM force feedback controller with guaranteed stability is synthesized in a way so as to contend with nonlinear PAM characteristics; 2) a mathematical tool is developed to compute reference PAM forces, for a given set of desired joint torque and joint stiffness inputs; and 3) on top of the torque controller, a position control scheme is implemented and its stability analysis is given in the sense of Lyapunov. In order to test the controller framework, an extensive set of experiments are conducted using an actuator that is constructed using two antagonistically coupled PAMs. As a result, the actuator exhibits satisfactory tracking performances concerning both torque–stiffness control and position–stiffness control modes.**

***Index Terms*—Compliant actuator, force and position control, pneumatic artificial muscle, variable stiffness.**

I. Introduction

INCORPORATION of passive compliance in modern-day actuators leads the way to the advancement of human-friendly robotics, a design and control concept in which humans and robots safely coexist and cooperate [1]–[3]. Contrary to the predominant robotics design approach, which makes use of nonbackdrivable and stiff actuators, this concept exploits the passivity properties of compliant actuators in a way so as to address stability, inherent safety, low output impedance, energy efficiency, and enhanced adaptability [1], [4]–[7]. Biological structures exploit this feature by means of adaptive control [8], [9], to create mechanically favorable energetics, and to stabilize unstable dynamics during environmental interactions [10], [11].

In the light of these shreds of evidence, a wide range of variable stiffness actuators has been developed for robotic applications [7], [12]. Within this context, pneumatic artificial muscles (PAMs) could exhibit advanced characteristics over electrical actuators [13], [14]. They possess superior power-to-weight ratios and have no requirement for heavy frictional gears [7]. Furthermore, the physical compliance property enables the incorporation of inherent safety and adaptivity; they can potentially emulate their biological counterparts in this sense. Although the constant need for pressurized air appears to be an inevitable drawback, PAMs were successfully employed in various robotic systems [15]–[21].

To name a few successful implementations, Zhao *et al.* exploited the physical compliance of PAMs for enhanced legged locomotion control [16]. Further implementations used the compliance property for advanced physical interactions in exoskeleton control [17], [18]. The researchers made use of pneumatic actuation to achieve active tactile sensing for soft morphological control in [19]. Ohta *et al.* developed a seven degrees of freedom (DoF) robot arm actuated via PAMs to ensure safe and dependable human–robot interaction [20]. For a more comprehensive review, one can refer to [21]. Therefore, it is evident that the PAMs have a wide range of applications in robotics because of their numerous favorable properties.

A pair of antagonistically coupled muscles could enable the simultaneous control of torque and stiffness [8], [9]. Despite the fact that PAMs can exhibit the variable stiffness behavior, this feature may not be sufficiently exploited in PAM-actuated robotics. In one of a few examples, Tondu and Lopez demonstrated that PAMs can be used as a torque and stiffness generator while using Hogan's model [22]. Bicchi and Tonietti utilized variable stiffness of PAMs while considering minimum-time optimal control with safety constraints [21]. Sardellitti *et al.* proposed a method to adjust stiffness by means of a sliding mode controller, applied to an average PAM-valve model [23].

Manuscript received October 19, 2018; revised March 14, 2019; accepted April 21, 2019. Date of publication May 10, 2019; date of current version December 3, 2019. This research was supported by the Commissioned Research of NICT, ImPACT of CSTI, NEDO, JST-Mirai Program No. JPMJMI18B8 Japan, and JSPS KAKENHI No. JP16H06565. Paper no. TII-18-2738. *(Corresponding author: Barkan Ugurlu.)*

B. Ugurlu is with the Department of Brain Robot Interface, Computational Neuroscience Laboratories, Advanced Telecommunications Research Institute International, Kyoto 619-0288, Japan, and also with the Department of Mechanical Engineering, Ozyegin University, Istanbul 34794, Turkey (e-mail: barkan.ugurlu@ozyegin.edu.tr).

P. Forni is with the Department of Brain Robot Interface, Computational Neuroscience Laboratories, Advanced Telecommunications Research Institute International, Kyoto 619-0288, Japan, and also with the Centre Automatique et Systemes, Mines-ParisTech, PSL Research University, 75006 Paris, France (e-mail: paolo.forni91@gmail.com).

C. Doppmann and J. Morimoto are with the Department of Brain Robot Interface, Computational Neuroscience Laboratories, Advanced Telecommunications Research Institute International, Kyoto 619-0288, Japan (e-mail: corinnedoppmann@gmx.ch; xmorimo@atr.jp).

E. Sariyildiz is with the School of Mechanical, Materials, Mechatronic and Biomedical Engineering, University of Wollongong, Wollongong, NSW 2522, Australia (e-mail: emre@uow.edu.au).

This paper has supplementary downloadable material available at http://ieeexplore.ieee.org, provided by the authors.

Color versions of one or more of the figures in this paper are available online at http://ieeexplore.ieee.org.

Digital Object Identifier 10.1109/TII.2019.2916228

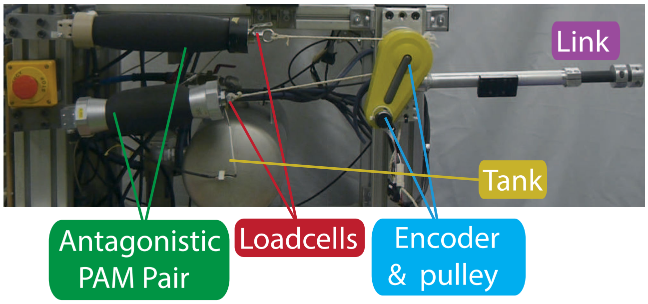

Fig. 1. Experimental test bench. Pressure servo valves are placed separately, and therefore, not displayed. The agonist muscle PAM-a is the one at the top; see Fig. 2.

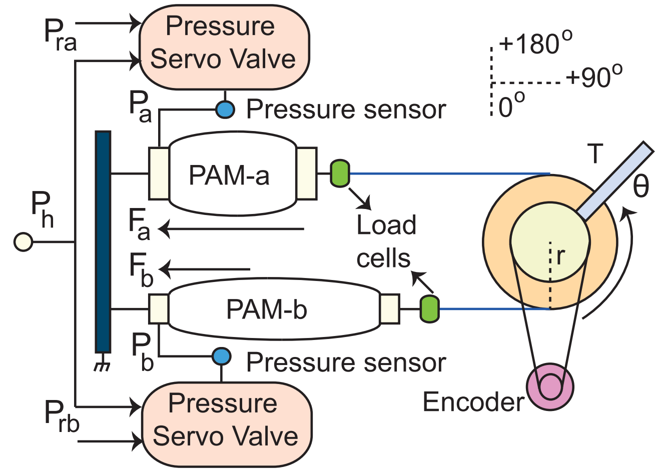

Fig. 2. Main elements of the experimental test bench. PAM-a is the agonist muscle, whereas PAM-b is the antagonist muscle.

Sharing the common ground with [8], this paper proposes a novel controller for an actuator that is powered via an antagonistically coupled PAM pair. The proposed controller can be stably configured in both simultaneous torque–stiffness control and simultaneous position–stiffness control modes. Despite several impressive studies, earlier reports may not fully address simultaneous control of force, position, and variable stiffness in terms of feedback control with proven stability conditions.

Within this context, this paper chiefly contributes toward this direction with the following qualities: 1) the synthesis of a stable PAM force feedback controller with proven passivity, so as to cope with nonlinear PAM characteristics; 2) a comprehensive mathematical model to interpret joint torque and variable torsional stiffness inputs in terms of individual muscle forces for achieving simultaneous torque and stiffness control mode; 3) a position and stiffness control mode with guaranteed stability considering multi-DoF dynamics, and 4) an extensive set of experiment tests concerning both control modes.

The paper is organized as follows. The hardware setup used in our experiments and our PAM modeling approach are succinctly introduced in Section II. Stable control modes (torque–stiffness control and position–stiffness control) are disclosed in Section III, together with their stability analyses. Experimental results are presented in Section IV. Section V concludes this paper.

II. Experimental Test Bench and PAM Modeling

One of the main objectives in our research of *soft* exoskeletons with an adjustable stiffness property, as they possess several advantages in terms of human–robot coexistence. To this end, a 1-DoF actuator module was developed to serve as an experimental test bench to evaluate the real-time performance of controllers; see Fig. 1.

The module was powered via a pair of antagonistically coupled PAMs (Festo MAS-40), including servo pressure valves (NORGREN, VP5010SBJ series, 0–8 bar) to control the inner pressure in proportion to the applied voltage inputs. PAMs were mechanically attached using a pulley–cable system. Cable lengths were adjusted while considering maximum PAM contraction and desired motion range: 60 to 110°; see Fig. 2. An encoder was deployed at the pulley to measure the actual joint angle, and therefore, PAM length variations. The valves can also output actual pressure measurements.

The maximum torque output is limited with ±60 N·m, by considering the maximum allowable force for the cable. Each PAM length is 22 cm when the input pressure is 0 bar; this drops to 15.5 cm when fully contracted. Custom-made hardware was used for control electronics. The sampling rate was kept at 250 Hz. In Fig. 2, F_a and F_b are PAM forces, measured via load cells (FUTEK, LCM300-FSH03755). P_a, P_b are measured pressure values, P_{ra}, P_{rb} are referential pressure values, T is the output torque produced by the actuator, r is the pulley radius, θ is the joint angle, and P_h is the supply pressure. A significantly rigid link is attached to the output of the actuator.

For PAM-powered actuators, one may construct a model to characterize the pressure-force-length relation mathematically. For this purpose, we combined the modeling approaches reported in [24]–[26] as follows:

$$F(P, L, \dot{L}) = P \sum_{\mathbf{u}=0}^{2} \mu_{\mathbf{u}} L^{\mathbf{u}} - \left(\sum_{\mathbf{j}=0}^{4} \eta_{\mathbf{j}} L^{\mathbf{j}} + \eta_5 L^{\frac{2}{3}} \right)$$
$$- \operatorname{sgn}(\dot{L}) \left(\lambda_2 \dot{L}^2 + \lambda_1 \dot{L} + \lambda_0 \left(1 - e^{-\frac{|\dot{L}|}{\lambda_3}} \right) \right) \quad (1)$$
$$= P\beta - \gamma. \quad (2)$$

In (1), P and L respectively denote PAM pressure and length, whereas F represents the PAM force generated due to contraction. $\beta = \beta(L)$ and $\gamma = \gamma(L, \dot{L})$ are used to arrange equations in a clear way. In order to obtain the coefficients in (1), namely, $\mu_{\mathbf{u}}$ ($\mathbf{u} = 0...2$), $\eta_{\mathbf{j}}$ ($\mathbf{j} = 0...5$), $\lambda_{\mathbf{k}}$ ($\mathbf{k} = 0...3$), a parameter identification routine was executed with 160000 collected samples of force, pressure, length, and length rate change. The coefficients may vary in the range of $\pm 10^6$. In this procedure, a chirp signal was assigned as the pressure input; its amplitude and frequency were varied between 0–8 bar and 0.1–4 Hz, respectively. Load

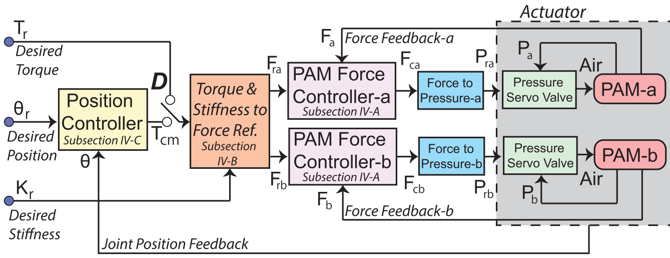

Fig. 3. Control framework, it is constituted as a cascaded architecture. The key D allows the choice between two control modes: 1) simultaneous torque–stiffness control, or 2) simultaneous position–stiffness control.

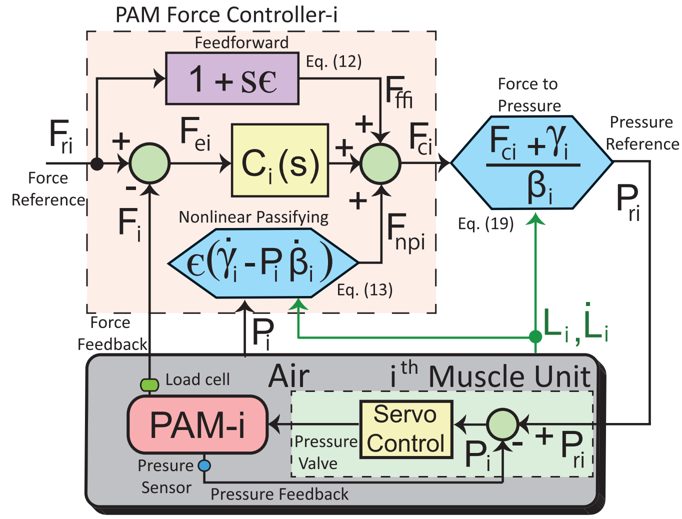

Fig. 4. Force feedback controller for a single PAM unit. The light pink block (PAM Force Controller-i) shows the details of the controller. See Fig. 3 for the role of this controller within the overall framework. The pressure valve, which is indicated via a light green block with a dashed frame, includes a built-in servo controller and is responsible for pressure tracking. It also provides pressure measurement: P_i. Blue heptagon blocks indicate function blocks. In the feedforward block, s is the Laplace variable to indicate time differentiation. Measurements of L_i and $\dot{L}_i$ are readily available via an encoder deployed in the joint unit; see Figs. 1 and 2.

cells, deployed at each PAM tip, were used to collect force data. Individual PAM lengths (L_a, L_b), were obtained using the actual joint angle

$$L_a = L_{0a} - r(\theta - \theta_0), \qquad L_b = L_{0b} + r(\theta - \theta_0) \tag{3}$$

where θ_0 is the initial joint angle when both PAM pressures at their minimum. L_{0a} and L_{0b} are the PAM length values when $\theta = \theta_0$. In fact, the PAM model comprises the cable in series, since the encoder at the joint is used to measure length L. This automatically allows us to incorporate cable stiffness in the model. A parameter identification procedure was performed via a nonlinear least-square fitting method. As a result, the maximum modeling error percentage stayed within the band of ±2.5%. For details concerning data collection, modeling, and tuning, refer to [27].

III. Control Framework

The controller framework is depicted in Fig. 3. In this figure, θ_r, θ, T_r, T_{cm}, and K_r indicate desired joint angle, actual joint angle, desired joint torque, command torque (position controller output), and desired joint stiffness, respectively. F_{ri}, F_i, F_{ci}, P_{ri}, and P_i sequentially denote desired force, actual force, command force (force controller output), reference pressure, and actual pressure for the ith PAM; $i = a, b$. Underscripts a and b, respectively, associate PAM parameters with agonist and antagonist muscle units.

The cascaded controller framework in Fig. 3 is sequentially constructed as follows.

1) To track desired force inputs, each PAM is controlled through a force feedback controller with guaranteed stability; see Section III-A.
2) Using this architecture, we develop a mathematical tool, which computes desired PAM forces (F_{ra}, F_{rb}) for a given set of desired joint torque input (T_r in torque control mode or T_{cm} in position control mode) and joint stiffness input (K_r); see Section III-B.
3) On top of the torque controller, a position control scheme is implemented; see Section III-C. In this case, variable stiffness control option is still viable, since the output of the position controller is linked to the torque input port.

The switch D in Fig. 3 allows the choice between two control modes: 1) simultaneous torque–stiffness control and 2) simultaneous position–stiffness control.

A. Stable Force Feedback for a Single Muscle

The ith PAM force feedback controller with guaranteed stability is illustrated in Fig. 4 [27]. Reference pressure inputs are inserted to proportional servo valves, as they ensure reliable pressure tracking control. Although we have no information regarding the servo valve inner control structure, we may use a linear first-order model to describe the mathematical relation between the reference pressure and actual pressure [23], [27]

$$\epsilon \dot{P}_i = -P_i + P_{ri}. \tag{4}$$

In (4), ϵ is the time constant, which can be experimentally characterized. P_{ri} is computed by inserting the ith force command F_{ci} to the related force–pressure model; see Fig. 3. The force–pressure model was given in (2). With this in mind, the combination of (2) and (4) yields the following:

$$\dot{P}_i = -\frac{P_i}{\epsilon} + \frac{F_{ci} + \gamma_i}{\epsilon \beta_i}. \tag{5}$$

Subtracting the actual force from the desired force outputs the force error, F_{ei}

$$F_{ei} = F_{ri} - F_i = F_{ri} - (P_i \beta_i - \gamma_i). \tag{6}$$

Despite the mapping $F_{ci} \mapsto F_{ei}$ is not passive, it is possible to render plant [see (5) and (6)] passive with respect to the mapping $\upsilon_i \mapsto F_{ei}$, in which υ_i is an external input to be defined. In this case, the storage function, $S(P)$, is assigned as follows:

$$S(P) = \frac{1}{2}\epsilon F_{ei}^2. \tag{7}$$

The first derivative of (7) is as follows:

$$\begin{aligned}\dot{S}(P) &= \epsilon F_{ei}\dot{F}_{ei} = \epsilon F_{ei}(\dot{F}_{ri} - \dot{F}_i) \\ &= \epsilon F_{ei}(\dot{F}_{ri} - \dot{P}_i\beta_i - P_i\dot{\beta}_i + \dot{\gamma}_i). \end{aligned} \tag{8}$$

Plugging (5) into (8)

$$\dot{S}(P) = F_{ei}(\epsilon(\dot{F}_{ri} - P_i\dot{\beta}_i + \dot{\gamma}_i) + P_i\beta_i - \gamma_i - F_{ci})) \tag{9}$$

and recalling that $F_i = P_i\beta_i - \gamma_i$

$$\dot{S}(P) = F_{ei}(\epsilon(\dot{F}_{ri} - P_i\dot{\beta}_i + \dot{\gamma}_i) + F_i - F_{ci}). \tag{10}$$

Command force (force controller output) F_{ci} is designated as follows:

$$F_{ci} = F_{ri} + \epsilon(\dot{F}_{ri} - P_i\dot{\beta}_i + \dot{\gamma}_i) - \upsilon_i. \tag{11}$$

In force command (11), υ_i is the external control input. $\epsilon(\dot{\gamma}_i - P_i\dot{\beta}_i)$ stands for nonlinear passifying terms, whereas $F_{ri} + \epsilon\dot{F}_{ri}$ indicate the feedforward input. They can be explicitly expressed as

$$F_{ffi} = F_{ri} + \epsilon\dot{F}_{ri} \tag{12}$$

$$F_{npi} = \epsilon(\dot{\gamma}_i - P_i\dot{\beta}_i) = \epsilon\left(\frac{\partial\gamma_i}{\partial L_i}\dot{L}_i - P_i\frac{\partial\beta_i}{\partial L_i}\dot{L}_i\right). \tag{13}$$

In (13), we utilized the chain rule to obtain $\dot{\gamma}_i$ and $\dot{\beta}_i$, since the rate change of PAM length $\dot{L}_i$ is readily available. Partial differentiations can be formulated with the help of (1) and (2)

$$\frac{\partial\gamma_i}{\partial L_i} = 4\eta_4 L_i^3 + 3\eta_3 L_i^2 + 2\eta_2 L_i + \eta_1 + \frac{2}{3}\eta_5 L_i^{-\frac{1}{3}} \tag{14}$$

$$\frac{\partial\beta_i}{\partial L_i} = 2\mu_2 L_i + \mu_1. \tag{15}$$

Placing (11) in (10), $\dot{S}(P)$ reduces to the following:

$$\begin{aligned}\dot{S}(P) &= F_{ei}(F_i - F_{ri} + \upsilon_i) = F_{ei}(-F_{ei} + \upsilon_i) \quad (16)\\ &= -F_{ei}^2 + F_{ei}\upsilon_i \le F_{ei}\upsilon_i. \quad (17)\end{aligned}$$

Equation (17) reveals that the plant (5), (6), along with the F_{ci} command that includes nonlinear passifying and feedforward terms, is a strictly passive system with respect to input υ_i and output F_{ei} [28]. Control input υ_i is constructed using a lead-lag controller; see $C_i(s)$ in Fig. 4

$$\upsilon_i = -F_{ei}C_i;\;\; C_i(s) = K_{xi}\Xi_i\frac{1 + T_{Ii}s}{1 + \Xi_i T_{Ii}s}\frac{1 + T_{Di}s}{1 + \alpha_i T_{Di}s}. \tag{18}$$

In (18), we have $0 \le T_{Di} < T_{Ii}$, $1 \le \Xi_i < \infty$, and $0 \le \alpha_i < 1$ [28]; $K_{xi}, T_{Di}, T_{Ii}, \Xi_i, \alpha_i$ are the controller gains that were tuned empirically according to standard rules of a linear controller design; stability and nonexcitation of unmodeled nonlinear dynamics. Their values are given in Table I for each PAM. Note that controller gains slightly differ for each PAM, since they have minor differences, e.g., length.

TABLE I
LEAD-LAG COMPENSATOR VALUES FOR EACH PAM UNIT

	K_{xi}	T_{Di}	T_{Ii}	Ξ_i	α_i
PAM-a	2.1	0.21	0.42	1.08	0.56
PAM-b	2.3	0.23	0.45	1.06	0.59

Finally, the force command F_{ci} can be converted to pressure commands for the servo valves by using (2) in reverse order:

$$P_{ri} = \frac{F_{ci} + \gamma_i}{\beta_i}. \tag{19}$$

One may wonder whether the passifying control command F_{ci} in (11) has actually provided a dynamic linearization via feedback. Indeed, by making use of (5), (6), and (11), the closed-loop systems read as follows:

$$\epsilon\dot{F}_{ei} = -F_{ei} + \upsilon_i. \tag{20}$$

It is then straightforward to design a linear controller to stabilize (20) to the origin $F_{ei} = 0$. Incorporating the nonlinear passifying terms and feedforward terms with the feedback control action ($F_{ei}C_i$) via (11) is the consequence of the stability analysis. In this case, the plant with the precompensator (the combination of nonlinear passifying and feedforward terms) and the controller establish a system with passive feedback interconnections. Referring to the direct implication given in (17) for this case, the system is asymptotically stable and bounded-input-bounded-output stable [28].

Synthesizing the controller using this theory not only proves the stability but also reveals a controller with high tracking performance thanks to nonlinear passifying and feedforward terms. The controller compensates certain nonlinearities that are intrinsic to PAM actuators, enabling our feedback controller to exhibit favorable tracking performance. In practice, the sole implementation of the classical feedback controllers (PID or lead-lag only, without feedforward and nonlinear passifying terms) revealed unacceptable tracking performance and frequently led to instability.

B. Torque and Variable Stiffness Control Mode

To achieve torque and stiffness control, we develop a mathematical tool that converts desired joint torque and variable stiffness (T_r, K_r) to reference PAM force inputs (F_{ra}, F_{rb}), for both agonist and antagonist muscles. In connection with Fig. 2, T_r may be obtained in terms of F_{ra} and F_{rb} as

$$T_r = r\left(F_{ra} - F_{rb}\right). \tag{21}$$

Desired joint stiffness, K_r, can be derived using a partial differentiation of (21) with respect to joint angle θ [8]. This approach may not characterize the effect of air flow; therefore, a certain amount of modeling uncertainty is present

$$K_r = \frac{\partial T_r}{\partial\theta} = r\left(\frac{\partial F_{ra}}{\partial L_a}\frac{\partial L_a}{\partial\theta} - \frac{\partial F_{rb}}{\partial L_b}\frac{\partial L_b}{\partial\theta}\right) \tag{22}$$

$$= r^2\left(\frac{\partial F_{ra}}{\partial L_a} + \frac{\partial F_{rb}}{\partial L_b}\right). \tag{23}$$

To yield (23), the chain rule is applied to (22) with (3) [23]. Evaluating (23), we need to differentiate force equations [see (1)] with respect to PAM lengths for the ith muscle unit

$$\begin{aligned} F_{ri} &= P_{ri} \sum_{\mathbf{u}=0}^{2} \mu_{\mathbf{u}i} L_i^{\mathbf{u}} - \sum_{\mathbf{j}=0}^{4} \eta_{\mathbf{j}i} L_i^{\mathbf{j}} - \eta_{5i} L_i^{\frac{2}{3}} \\ &\quad - \operatorname{sgn}(\dot{L}_i)\left(\sum_{\mathbf{k}=0}^{2} \lambda_{\mathbf{k}i} \dot{L}_i^{\mathbf{k}} + \lambda_{3i} e^{-\frac{|\dot{L}_i|}{\lambda_{4i}}}\right) && (24) \\ &= P_{ri}\beta_i - \gamma_i && (25) \end{aligned}$$

$$\begin{aligned} \frac{\partial F_{ri}}{\partial L_i} &= P_{ri} \sum_{\mathbf{u}=1}^{2} \mathbf{u} \mu_{\mathbf{u}i} L_i^{\mathbf{u}-1} + \frac{\partial P_{ri}}{\partial L_i}\beta_i \\ &\quad - \sum_{\mathbf{j}=1}^{4} \mathbf{j} \eta_{\mathbf{j}i} L_i^{\mathbf{j}-1} - \frac{2}{3}\eta_{5i} L_i^{-\frac{1}{3}} && (26) \\ &= P_{ri}\Phi_i + \frac{\partial P_{ri}}{\partial L_i}\beta_i - \Psi_i. && (27) \end{aligned}$$

In (24) and (26), $\mu_{\mathbf{u}i}$ ($\mathbf{u} = 0..2$), $\eta_{\mathbf{j}i}$ ($\mathbf{j} = 0...5$), and $\lambda_{\mathbf{k}i}$ ($\mathbf{k} = 0...4$) are PAM model parameters and identified for both muscles. The functions β_i, γ_i, Φ_i, and Ψ_i are used to clarify the notation. In addition, $\frac{\partial P_{ri}}{\partial L_i}$ term is insignificant when the actuator volume is much smaller than the air tank volume[15], [23]. Therefore, $\frac{\partial P_{ri}}{\partial L_i}\beta_i$ term is practically negligible. In [27], an attempt for this formulation included a misconception; yet, the corresponding error was observed to be insignificant

$$K_r = r^2\left(\frac{\Phi_a}{\beta_a}(F_{ra} + \gamma_a) + \frac{\Phi_b}{\beta_b}(F_{rb} + \gamma_b) - \Psi_b - \Psi_a\right). \quad (28)$$

Equations (21) and (28) constitute a set of formulae to compute joint torque and stiffness, in terms of PAM forces. Since our main purpose is to obtain PAM forces in terms of joint torque and stiffness, (21) and (28) are solved to obtain PAM forces. As such, the following computation is performed:

$$\begin{aligned} F_{ra} &= \frac{\beta_a\beta_b}{\Phi_a\beta_b + \Phi_b\beta_a}\left(\frac{K_r}{r^2} + \Psi_b + \Psi_a - \frac{\Phi_a}{\beta_a}\gamma_a \right. \\ &\qquad \left. - \frac{\Phi_b}{\beta_b}\left(\gamma_b - \frac{T_r}{r}\right)\right) && (29) \\ F_{rb} &= F_{ra} - \frac{T_r}{r}. && (30) \end{aligned}$$

C. Position and Variable Stiffness Control Mode

The torque controller described in Section III-B enables us to construct a reliable position control scheme on top of it. To attain this goal, we make use of the computed torque control [29] whose block diagram is displayed in Fig. 5. In this figure, the trajectory planner is responsible for the generation of reference joint angles (q_r), depending on the task-specific robot motion. The controller makes use of robot dynamics; therefore, the position control performance can be enhanced.

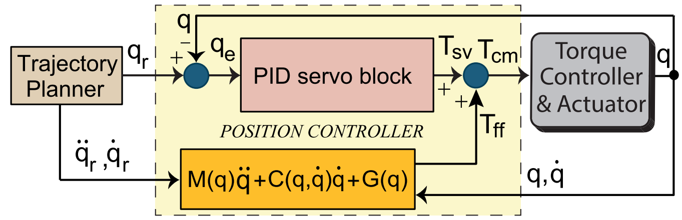

Fig. 5. Computed torque control with PID is chosen as the position controller. The light yellow block corresponds to the position control block in Fig. 3. For clarity, the rest of the blocks concerning the torque and stiffness to PAM forces, individual PAM force controllers, and the actuator are summed up within the gray block, named "Torque Controller and Actuator."

Although the hardware setup we use in our experiments is 1-DoF, we present a stability proof for a multi-DoF system to show the generality of the controller. Thus, we use the *so-called* reduced flexible multi-DoF robot dynamics [30]:

$$M(q)\ddot{q} + C(q,\dot{q})\dot{q} + G(q) = T + T_{ext} \quad (31)$$
$$T_{cm} = T - Kq - B_p\dot{q} - J_p\ddot{q}. \quad (32)$$

In (31) and (32), $M(q)$, and $G(q)$, and $C(q,\dot{q})$ are inertial, gravity, and coriolis and centrifugal terms, respectively. T is the output torque, q is the joint angle vector, $T_{\rm cm}$ is the task-specific command torque (the output of the position controller in this case), and $T_{\rm ext}$ is the external disturbance torque. K, B_p, and J_p are diagonal matrices that represent joint stiffness, pulley friction, and pulley inertia. Since there are no gear nor mechanical transmission, B_p is negligibly small. J_p is also very small and omitted. Keeping this in mind, the combination of (31) and (32) yields the following:

$$M(q)\ddot{q} + C(q,\dot{q})\dot{q} + G(q) - Kq - T_{\rm cm} - T_{\rm ext} = 0. \quad (33)$$

Utilizing the following computed torque control, $T_{\rm cm}$ is defined as

$$\begin{aligned} T_{\rm cm} &= G(q) + M(q)\ddot{q}_r \\ &\quad + K_p q_e + K_v \dot{q}_e + K_i \int_0^t q_e \, dt + C(q,\dot{q})\dot{q}_r. && (34) \end{aligned}$$

The joint angle error is q_e, which is obtained via $q_e = q_r - q$. K_p and K_i and K_v are diagonal matrices that store positive PID gains. Plugging (34) into (33) results as follows:

$$M(q)\ddot{q}_e + (C(q,\dot{q}) + K_v)\dot{q}_e + (K_p - K)q_e = \tilde{\nu} \quad (35)$$

where $\tilde{\nu} := \nu + d$, $d := -Kq_r - T_{\rm ext}$, and $\nu := -K_i \int_0^t q_e \, dt$.

We are now going to prove that, for any basin of attraction $\Omega_l := \left\{(q_e, \dot{q}_e, \tilde{\nu}) \in \mathbb{R}^{3n} : \|(q_e, \dot{q}_e, \tilde{\nu})\| \le l\right\}$ $q_r(t), T_{ext}(t)$, we can always select PID gains K_p, K_i, K_v such that, for any constant $d(t), t \ge 0$ and for any initial condition in Ω_l, the error dynamics converges to zero, i.e., $(q_e(t), \dot{q}_e(t)) \to 0$ as $t \to +\infty$.

To this end, we propose a Lyapunov function candidate as follows [31]:

$$V = \frac{1}{2}\dot{q}_e^\top M(q)\dot{q}_e + \frac{1}{2}q_e^\top\left(K_p - K - \frac{1}{\varepsilon}K_i\right)q_e + \varepsilon q_e M(q)\dot{q}_e + \frac{\varepsilon}{2}\left(-\frac{1}{\varepsilon}K_i q_e + \tilde{\nu}\right)^\top K_i^{-1}\left(-\frac{1}{\varepsilon}K_i q_e + \tilde{\nu}\right) \tag{36}$$

which is positive definite and radially unbounded on Ω_l when ε is sufficiently small. Furthermore, K_p and K_i gains are properly tuned so as to ensure $\varepsilon(K_p - K) - K_i$ is positive definite.

By taking the time derivative of V along the solutions of (35), we have

$$\dot{V} = -\begin{pmatrix}\dot{q}_e\\ q_e\end{pmatrix}^\top \underbrace{\begin{pmatrix} K_v - \varepsilon M & \frac{\varepsilon}{2}(K_v - C^\top)\\ \frac{\varepsilon}{2}(K_v - C) & \varepsilon(K_p - K) - K_i\end{pmatrix}}_{A(q,\dot{q})}\begin{pmatrix}\dot{q}_e\\ q_e\end{pmatrix} \tag{37}$$

where we made use of the skew symmetry property $\dot{M} - 2C$.

The $A(q,\dot{q})$ is positive definite on Ω_v when the following Schur complement conditions are met:

$$\varepsilon(K_p - K) - K_i \succ N \succ 0 \tag{38}$$

$$K_v \succ \varepsilon m_2 I + \frac{\varepsilon^2}{4}\left(K_v - C^\top\right)N^{-1}\left(K_v - C^\top\right) \tag{39}$$

where N is an arbitrary positive definite matrix. Furthermore, $m_1 I < M < m_2 I$ in which m_1 and m_2 are nonnegative scalar numbers and I is an identity matrix with proper dimension; $|C(q,\dot{q})| < k_c|\dot{q}_e| < k_l$ where k_c and k_l are nonnegative scalar numbers. PID gains are empirically tuned in accordance with the above convergence analysis such that (36), (38), and (39) hold true. Therefore, by a direct application of LaSalle's principle, we conclude that $q_e(t), \dot{q}_e(t) \to 0$ as $t \to +\infty$. For our case, these gains are assigned as $K_p = 166.67$, $K_i = 2.83$, and $K_v = 4.17$.

IV. Experiment Results

All the experiments were conducted on the 1-DoF test bench; see Section II. Because of safety precautions, input characteristics were kept within certain limits in a way that force references do not exceed 1600 N. Refer to the multimedia attachment to view certain scenes from the experiments.

A. Force Control

As explained previously, simultaneous position/torque and variable stiffness control problems were converted to individual PAM force control. Therefore, it is of importance to ensure reliable force tracking for each muscle. To this end, we conducted force control experiments on a single PAM unit and compared its performance with respect to the conventional method in which a PID+Feedforward controller was utilized [22]. The gains of the conventional controller were empirically tuned, i.e., they were set for the maximum possible performance without causing unstable oscillations. The results are plotted in Figs. 6–8.

In Fig. 6, a step input with an amplitude of 700 N was implemented as the force reference and it is indicated via a blue dash-dotted line. The response of the proposed and conventional

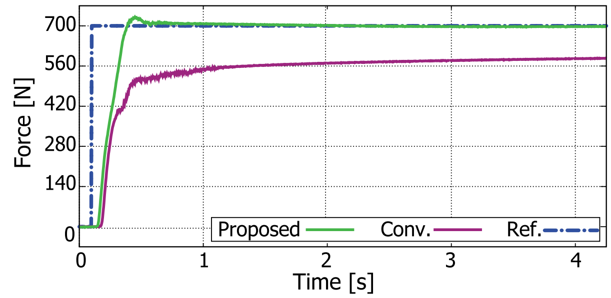

Fig. 6. Force control results for a step input with an amplitude of 700 N.

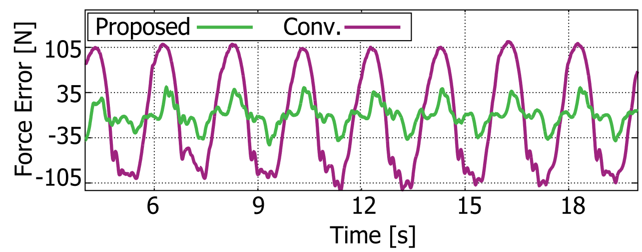

Fig. 7. Force tracking error graphics for a sine wave input at 0.5 Hz.

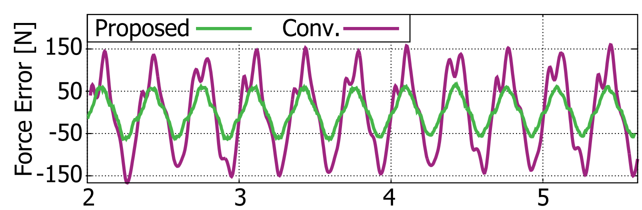

Fig. 8. Force tracking error graphics for a sine wave input at 2.0 Hz.

controllers are respectively plotted via solid green and purple lines. As may be observed, the proposed controller exhibited a good performance; it converged to the reference with a settling time of 0.5 s and 5% overshoot. The steady-state error was measured to be approximately 5 N. For the case of conventional controller, the steady-state error was approximately 110 N. It also converged to a constant value after 1.9 s.

In Figs. 7 and 8, sine input signals were implemented. The frequency of the sine wave was 0.5 Hz in Fig. 7 and 2.0 Hz in Fig. 8. Force tracking error signals were depicted via solid green and purple lines for the proposed and conventional controllers, respectively. For the case of conventional controller, the force error stayed within ±105 and ±150 N bands for 0.5 and 2.0 Hz input signals, respectively. On the contrary, the proposed controller exhibited more favorable results and reduced the force tracking error for about 67% in each case.

The proposed force controller can take PAM nonlinearities into account, and therefore, outperformed the conventional controller. Therefore, it provided a solid basis to establish simultaneous position/torque and variable stiffness control. As the proposed controller includes a feedback linearization loop (nonlinear passifying terms), it had a larger control bandwidth. In contrast, we had a relatively more limited bandwidth in the case of the conventional controller as it does not comprise nonlinear terms.

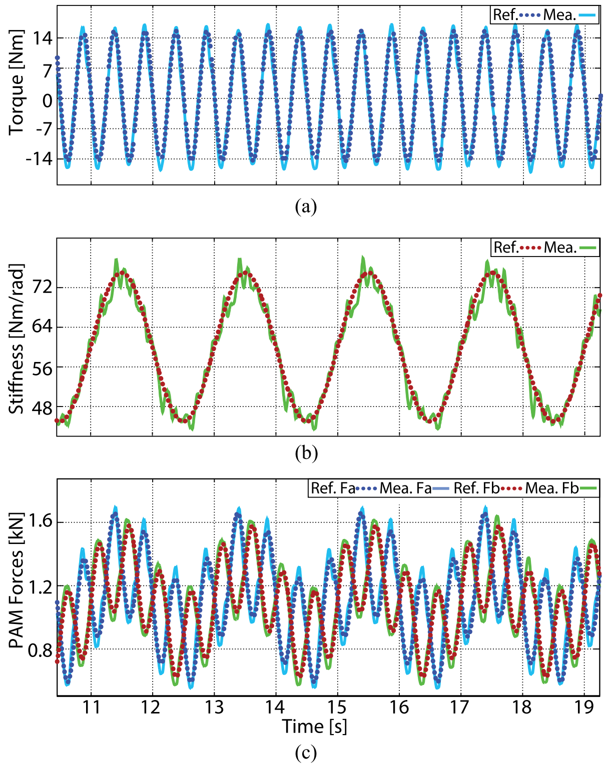

Fig. 9. (a) Torque tracking results for a sine wave input at 2.0 Hz. (b) Stiffness tracking results for a sine wave input at 0.5 Hz. (c) Individual PAM force tracking results. F_a and F_b stand for agonist and antagonist muscle forces, respectively; see Fig. 2. The torque input signal frequency was greater than the stiffness input signal frequency; 2.0 Hz $>$ 0.5 Hz.

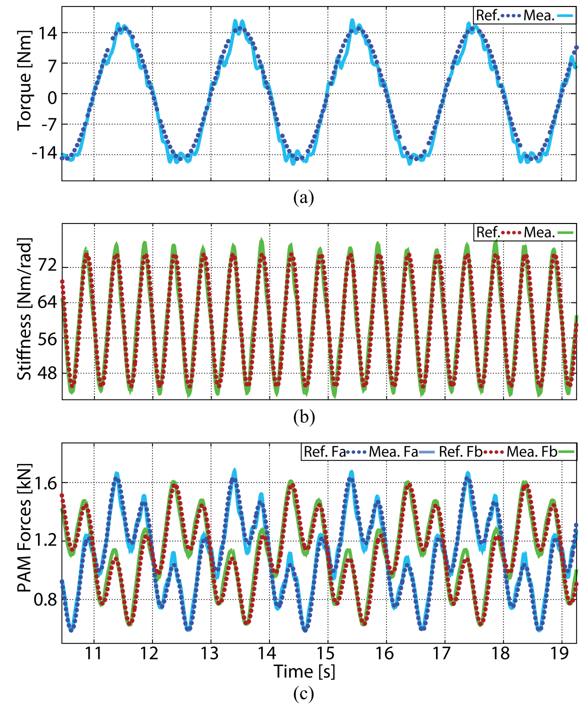

Fig. 10. (a) Torque tracking results for a sine wave input at 0.5 Hz. (b) Stiffness tracking results for a sine wave input at 2.0 Hz. (c) Individual PAM force tracking results. F_a and F_b stand for agonist and antagonist muscle forces, respectively; see Fig. 2. The stiffness input signal frequency was greater than the torque input signal frequency 2.0 Hz $>$ 0.5 Hz.

B. Simultaneous Torque and Stiffness Control

Simultaneous torque and variable stiffness tracking control experiment results are presented in Figs. 9(a) and (b) and 10(a) and (b), in which dotted blue and solid cyan and dotted red and solid green lines, respectively, indicate reference and response torque and stiffness variations.

In Fig. 9(a), torque reference input was a sine wave signal with a frequency of 2.0 Hz and with a peak-to-peak amplitude of 30 ($\pm$15) N·m. In Fig. 9(b), stiffness reference input was a sine wave with a frequency of 0.5 Hz and a peak-to-peak amplitude of 30 (60 $\pm$ 15) N·m/rad. In this experiment, the torque input frequency was chosen differently than the stiffness input frequency; 2.0 Hz $>$ 0.5 Hz. Despite the difference in input frequencies, the controller showed a satisfactory performance, concerning both joint torque and joint stiffness tracking.

Fig. 10(a) and (b) depict simultaneous torque and stiffness tracking results from a similar experiment. In contrast to the previous experiment, torque and stiffness reference input frequencies were assigned as 0.5 and 2.0 Hz, respectively; 0.5 Hz $<$ 2.0 Hz. Amplitudes were kept the same as in the previous experiment. Similar to the previous case, the controller exhibited favorable tracking performances regarding the simultaneous joint torque and stiffness control.

Force tracking performances of each PAM are displayed in Figs. 9(c) and 10(c). Agonist muscle (PAM-a) reference and measured forces are represented via dotted blue and solid cyan lines. Antagonist muscle (PAM-b) reference and actual forces are indicated with dotted red and solid green lines. Scrutinizing Fig. 9(c), one can observe that the PAM force references appear to be the interference pattern of two input frequencies, namely, torque input (2.0 Hz) and stiffness input (0.5 Hz). A similar case with a different interference pattern may be observed in Fig. 10(c) as well. In both cases, force references were tracked well, thanks to the stabilized force control strategy. It is the force feedback controller (see Fig. 4) that ensures the simultaneous torque and stiffness control, simply by tracking the individual PAM force references.

C. Position Control Experiments: Constant Stiffness

In order to solely display position control with constant stiffness, we conducted joint tracking experiments with a 2.5-kg dumbbell, which is attached to the actuator tip as the payload.

Fig. 11 displays position tracking performances when the stiffness reference is set to a constant value. One can assign this value freely within the physical limits. In our experiments, it was 65 N·m/rad. In this figure, dotted blue and solid cyan lines, respectively, stand for reference and measured joint position variations. Actual joint angles were measured via the encoder. In Fig. 11(a), the input signal was a sine wave at 0.5 Hz with a peak-to-peak amplitude of 40° (65°$\sim$105°). In Fig. 11(b), the input frequency was 2.5 Hz and had a peak-to-peak amplitude of 10° (85°$\sim$95°). The amplitude was deliberately kept low for 2.5 Hz input to ensure safety during the experiment. Fig. 11

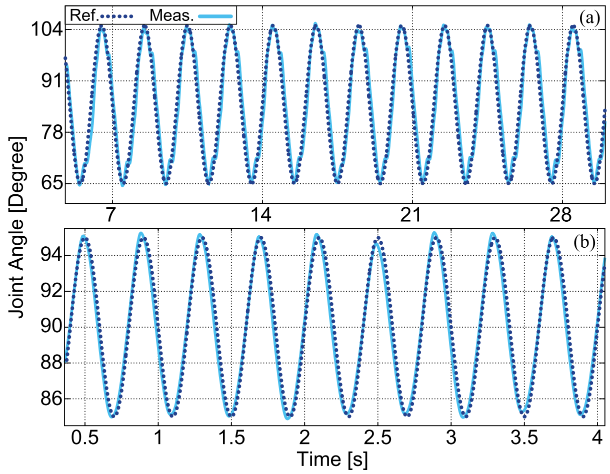

Fig. 11. Position tracking when the stiffness was set to 65 N·m/rad. (a) Sine wave with an input frequency of 0.5 Hz. (c) Sine wave with an input frequency of 2.5 Hz.

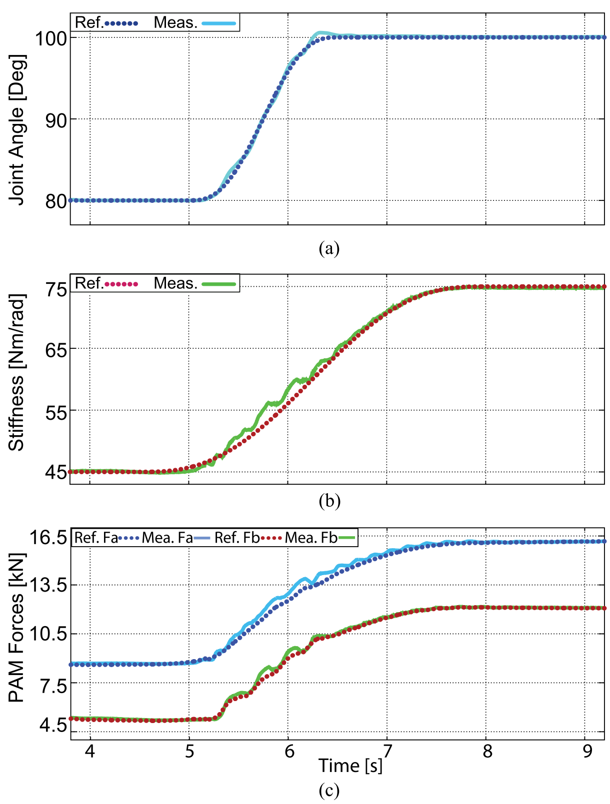

Fig. 12. Position and stiffness tracking results for inputs generated via fifth-order polynomials. (a) Position reference trajectory started from 80° when $t = 5.3$, and arrived at 100° when $t = 6.5$. (b) Stiffness reference trajectory started from 45 N·m/rad when $t = 5.0$, and arrived at 75 N·m/rad when $t = 7.5$. (c) Force profile and tracking of each muscle to execute this motion.

indicates that the position tracking was satisfactory and assured for both low- and high-frequency reference inputs.

D. Simultaneous Position and Stiffness Control

In Figs. 12(a) and (b) and 13(a) and (b), simultaneous position and stiffness tracking plots are displayed, where dotted blue, solid cyan, dotted purple, and solid green lines, respectively, point out reference joint position, actual joint position, reference joint stiffness, and response joint stiffness. In Figs. 12(c) and 13(c), force tracking performances can be examined for each PAM unit. Agonist muscle (PAM-a) reference and measured forces are represented via dotted blue and solid cyan lines. Antagonist muscle (PAM-b) reference and actual forces are indicated with dotted red and solid green lines.

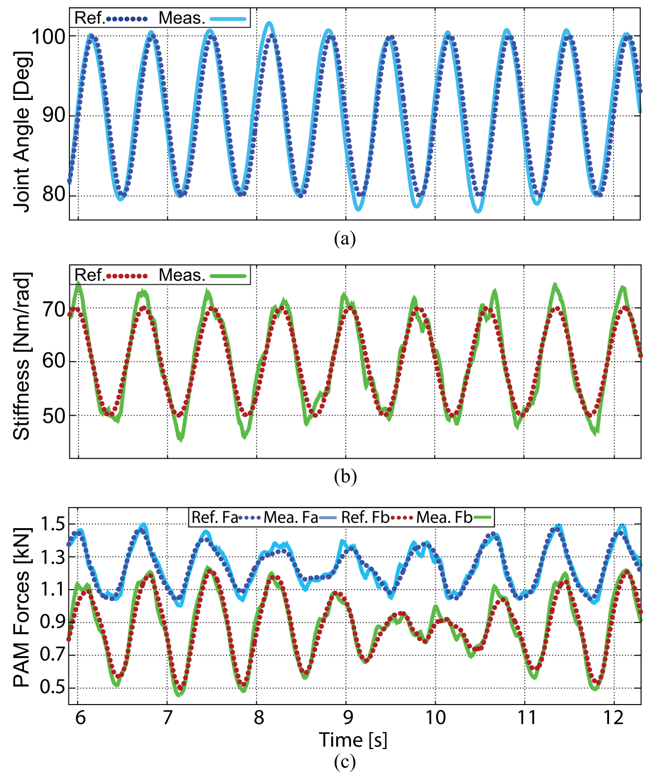

Fig. 13. Position and stiffness tracking results for inputs generated sine waves. (a) Position reference input at 1.5 Hz with a peak-to-peak amplitude of 20°. (b) Stiffness reference input at 0.8 Hz with a peak-to-peak amplitude of 20 N·m/rad. (c) Force profile and tracking of each muscle to execute this motion.

For the results included in Fig. 12(a) and (b), position and stiffness inputs were generated via fifth-order polynomials. The position reference trajectory started from 80° when $t = 5.3$, and arrived at 100° when $t = 6.5$. Stiffness reference trajectory started from 45 N·m/rad when $t = 5.0$, and arrived at 75 N·m/rad when $t = 7.5$. In conclusion, we obtained satisfactory position and variable stiffness tracking performances, despite a minor fluctuation in stiffness tracking. Once the trajectories were ended, both stiffness and position values settled to their terminal references. In this particular experiment, the stiffness trajectory period was deliberately chosen longer than the position trajectory; however, an inverse pattern can also be successfully realized in our system without any restriction.

In Fig. 13(a) and (b), position and stiffness inputs were generated via sine waves. Position and stiffness reference input frequencies were 1.5 and 0.8 Hz, respectively. Peak-to-peak amplitudes of these inputs were 20° (80° $\sim$ 100°), and 20 N·m/rad (50$\sim$70 N·m/rad). Observing this figure, we can see that the controller provided favorable position and variable stiffness tracking performances, despite the fact that input frequencies were chosen differently.

The output of the position controller is the torque command; see Fig. 5. Therefore, individual PAM reference forces are the interference pattern of the command torque and stiffness inputs. With this in mind, we added force tracking results for each muscle unit in Figs. 12(c) and 13(c). Similarly, agonist muscle (PAM-a) reference and measured forces are represented via dotted blue and solid cyan lines. Antagonist muscle (PAM-b) reference and actual forces are indicated with dotted red and solid green lines. These results show that the individual PAM force tracking was assured as well, both for polynomial and sinusoidal position and stiffness inputs.

V. Conclusion

In this paper, we proposed a novel controller framework for actuators, powered via antagonistically driven pneumatic artificial muscles. The controller can be configured in two stable control modes: 1) simultaneous torque and variable stiffness control, and 2) simultaneous position and variable stiffness control. Using a detailed model that encapsulates intrinsic PAM nonlinearities (friction and nonlinear elasticity), and synthesizing effective control techniques that account for those nonlinearities, the actuator exhibited favorable tracking performances in both control modes. An extensive set of hardware experiments validated the controller, as the actuator exhibited favorable tracking performances when configured in both control modes.

In constructing this controller, three main contributions were offered.

1) A PAM force feedback controller with guaranteed stability was synthesized using the dissipativity theory. The controller was able to cope with the inherent nonlinearities of PAMs, which occur due to frictional and nonlinear elasticity terms.
2) On the basis of a detailed PAM model, a set of equations was derived to compute PAM force references, which correspond to desired joint torque and stiffness inputs. Together with the stable PAM force feedback controller, this strategy allowed us to associate feedback control for the simultaneous torque–stiffness control task.
3) As we obtained a reliable torque controller, a position controller that is compatible with multi-DoF robots was derived and its stability conditions were demonstrated via Lyapunov's theory.

Since PAMs can generate only unidirectional forces, it is a strict obligation to use antagonistic setups to create bidirectional joint torque. Therefore, there is an actuator redundancy for this type of actuators. We believe that controlling the variable stiffness is a very efficient way of exploiting this redundancy, as PAMs have nonlinear elasticity characteristics. Simultaneous torque and stiffness control is also observed in biological structures as well; they tune the muscle impedance characteristics by means of adaptive control to maintain stable postures and optimize mechanical energetics [9]–[11]. Considering this fact, PAM-powered actuators with variable stiffness control option can emulate biological muscles in this manner.

One particular aspect that was observed in the overall controller performance is that stiffness control may be slightly out of the track during dynamic transitioning. This may be due to the fact that the stiffness controller does not have direct sensory feedback. Unlike stiffness, torque and position can be directly measured and fed back via load cells and encoders. However, stiffness tracking solely relies on model-based stiffness-force transformation and inner force control loops. One possible way to remedy this issue may be the utilization of stiffness sensors [32]. In order to further improve the tracking controllers, one may increase the sampling frequency and use sensors with higher resolution so that PAM force controller performance can be enhanced.

When performing simultaneous control, it is observed that the low-frequency input has high-frequency harmonics, which may arise due to unmodeled coupling effects. Although the amplitude of these harmonics is well contained, one can eliminate these harmonics by using more comprehensive modeling approaches. Therefore, this issue is addressed as a future work.

Already, our research group implemented the proposed controllers to our multi-DoF exoskeleton systems, powered via PAMs, so as to address robot-aided rehabilitation, power augmentation, and active walking assist studies in rehabilitation centers [17]. Our next work will focus on the exploitation of adjustable stiffness feature for robot-aided neuro-rehabilitation applications in terms of inherently safe, synergistic, and stable human–robot interaction.

References

[1] M. Zinn, O. Khatib, B. Roth, and J. K. Salisbury, "Playing it safe [human-friendly robot]," *IEEE Robot. Autom. Mag.*, vol. 11, no. 2, pp. 12–21, Jun. 2004.

[2] C. Yang, C. Zeng, Y. Cong, N. Wang, and M. Wang, "A learning framework of adaptive manipulative skills from human to robot," *IEEE Trans. Ind. Informat.*, vol. 15, no. 2, pp. 1153–1161, Feb. 2019.

[3] L. Roveda, G. Palluca, N. Pedrocchi, F. Braghin, and L. M. Tosatti, "Iterative learning procedure with reinforcement for high-accuracy force tracking in robotized tasks," *IEEE Trans. Ind. Informat.*, vol. 14, no. 4, pp. 1753–1763, Apr. 2018.

[4] Y. Yunda, C. Zhang, A. Narayan, J. Yang, S. Li, and H. Yu, "Generalized dynamic predictive control for non-parametric uncertain systems with application to series elastic actuators," *IEEE Trans. Ind. Informat.*, vol. 14, no. 11, pp. 4829–4840, Nov. 2018.

[5] W. He, Y. Ouyang, and J. Hong, "Vibration control of a flexible robotic manipulator in the presence of input deadzone," *IEEE Trans. Ind. Informat.*, vol. 13, no. 1, pp. 48–59, Feb. 2017.

[6] C. Li, X. Gu, X. Xiao, C. M. Lim, and H. Ren, "A robotic system with multi-channel flexible parallel manipulators for single port access surgery," *IEEE Trans. Ind. Informat.*, vol. 15, no. 3, pp. 1678–1687, Mar. 2019.

[7] R. Van Ham, T. G. Sugar, B. Vanderborght, K. W. Hollander, and D. Lefeber, "Compliant actuator designs," *IEEE Robot. Autom. Mag.*, vol. 16, no. 3, pp. 81–94, Sep. 2009.

[8] N. Hogan, "Adaptive control of mechanical impedance by coactivation of antagonist muscles," *IEEE Trans. Autom. Control*, vol. 29, no. 8, pp. 681–690, Aug. 1984.

[9] H. Lee, H. I. Krebs, and N. Hogan, "Multivariable dynamic ankle mechanical impedance with active muscles," *IEEE Trans. Rehabil. Eng.*, vol. 22, no. 5, pp. 971–981, Sep. 2014.

[10] W. A. Farahat and H. Herr, "Optimal workloop energetics of muscle-actuated systems: An impedance matching view," *PLOS Comput. Biol.*, vol. 6, no. 6, pp. 1–11, 2010.

[11] E. Burdet, R. Osu, D. Franklin, T. E. Milner, and M. Kawato, "The central nervous system stabilizes unstable dynamics by learning optimal impedance," *Nature*, vol. 414, no. 6862, pp. 446–449, 2001.

[12] E. Sariyildiz, G. Chen, and H. Yu, "Robust trajectory tracking control of multimass resonant systems in state space," *IEEE Trans. Ind. Electron.*, vol. 64, no. 12, pp. 9366–9377, Dec. 2017.

[13] L. Zhao, H. Cheng, Y. Xia, and B. Liu, "Angle tracking adaptive backstepping control for a mechanism of pneumatic muscle actuators via an AESO," *IEEE Trans. Ind. Electron.*, vol. 66, no. 6, pp. 4566–4576, Jun. 2019.

[14] L. Zhu, X. Shi, Z. Chen, H.-T. Zhang, and C.-H. Xiong, "Adaptive servomechanism of pneumatic muscle actuators with uncertainties," *IEEE Trans. Ind. Electron.*, vol. 64, no. 4, pp. 3329–3337, Apr. 2017.

[15] R. W. Colbrunn, G. M. Nelson, and R. D. Quinn, "Modeling of braided pneumatic actuators for robotic control," in *Proc. IEEE Conf. Intell. Robots Syst.*, Maui, HI, USA, 2001, pp. 1964–1970.

[16] Q. Zhao, B. Ellenberger, H. Sumioka, T. Sandy, and R. Pfeifer, "The effect of spine actuation and stiffness on a pneumatically-driven quadruped robot for cheetah-like locomotion," in *Proc. IEEE Conf. Robot. Biomimetics*, Shenzen, China, 2013, pp. 1807–1812.

[17] B. Ugurlu *et al.*, "Variable ankle stiffness improves balance control: Experiments on a bipedal exoskeleton," *IEEE Trans. Mechatronics*, vol. 21, no. 1, pp. 79–87, Feb. 2016.

[18] D. Sasaki, T. Noritsugu, and M. Takaiwa, "Development of pneumatic lower limb power assist wear driven with wearable air supply system," in *Proc. IEEE Conf. Intell. Robots Syst.*, Tokyo, Japan, 2013, pp. 4440–4445.

[19] V. A. Ho, H. Yamashita, Z. Wang, S. Hirai, and K. Shibuya, "Wrin'Tac: Tactile sensing system with Wrinkle's morphological change," *IEEE Trans. Ind. Informat.*, vol. 13, no. 5, pp. 2496–2506, Oct. 2017.

[20] P. Ohta *et al.*, "Design of a lightweight soft robotic arm using pneumatic artificial muscles and inflatable sleeves," *Soft Robot.*, vol. 5, no. 2, pp. 1–12, 2018.

[21] A. Bicchi and G. Tonietti, "Fast and 'soft-arm' tactics [robot arm design]," *IEEE Robot. Autom. Mag.*, vol. 11, no. 2, pp. 22–33, Jun. 2004.

[22] B. Tondu and P. Lopez, "Modeling and control of McKibben artificial muscle robot actuators," *IEEE Control Syst. Mag.*, vol. 20, no. 2, pp. 15–38, Apr. 2000.

[23] I. Sardellitti, G. Palli, N. G. Tsagarakis, and D. G. Caldwell, "Antagonistically actuated compliant joint: Torque and stiffness control," in *Proc. IEEE Conf. Intell. Robots Syst.*, Taipei, Taiwan, 2010, pp. 1909–1914.

[24] C.-P. Chou and B. Hannaford, "Measurement and modeling of McKibben pneumatic artificial muscles," *IEEE Trans. Robot. Autom.*, vol. 12, no. 1, pp. 90–102, Feb. 1996.

[25] A. Hildebrandt, O. Sawodny, R. Neumann, and A. Hartmann, "Cascaded control concept of a robot with two degrees of freedom driven by four artificial pneumatic muscle actuators," in *Proc. IEEE Conf. Am. Control Conf.*, Portland, OR, USA, 2005, pp. 680–685.

[26] B. Tondu, "Closed-loop position control of artificial muscles with a single integral action: Application to robust positioning of McKibben artificial muscle," *Proc. IEEE Conf. Mechatronics*, Vicenza, Italy, 2013, pp. 718–723.

[27] B. Ugurlu, P. Forni, C. Doppmann, and J. Morimoto, "Torque and variable stiffness control for antagonistically driven pneumatic muscle actuators via a stable force feedback controller," in *Proc. IEEE Conf. Intell. Robots and Syst.*, Hamburg, Germany, 2015, pp. 1633–1639.

[28] B. Brogliato, R. Lozano, B. Maschke, and O. Egeland, *Dissipative Systems Analysis and Control: Theory and Applications.* London, U.K.: Springer, 2010.

[29] T. G. Thuruthel, Y. Ansari, E. Falotico, and C. Laschi, "Control strategies for soft robotic manipulators: A survey," *Soft Robot.*, vol. 5, no. 2, pp. 1–12, 2018.

[30] G. Buondonno and A. De Luca, "A recursive Newton-Euler algorithm for robots with elastic joints and its application to control," in *Proc. IEEE Conf. Intell. Robots Syst.*, Hamburg, Germany, 2015, pp. 5526–5532.

[31] R. Ortega, A. Loria, and R. Kelly, "A semiglobally stable output feedback PI2D regulator for robot manipulators," *IEEE Trans. Autom. Control*, vol. 40, no. 8, pp. 1432–1436, Sep. 1995.

[32] T.-V. Nguyen, R. Tanii, T. Takahata, and I. Shimoyama, "Development of a single-chip elasticity sensor using MEMS-based piezoresistive cantilevers with different tactile properties," *Sens. Actuators A, Phys.*, vol. 285, pp. 362–368, 2019.

Barkan Ugurlu (S'08–M'10) received the Ph.D. degree in electrical and computer engineering from Yokohama National University, Yokohama, Japan, in 2010.

From 2010 to 2013, he was a Postdoctoral Researcher with the Istituto Italiano di Tecnologia, Genova, Italy, and Toyota Technological Institute, Nagoya, Japan. From 2013 to 2015, he was a Research Scientist with the Computational Neuroscience Laboratories, ATR, Kyoto, Japan. He is a Marie Sklodowska-Curie Fellow and currently holds an Assistant Professor position with the Department of Mechanical Engineering, Ozyegin University, Istanbul, Turkey.

Paolo Forni received the Ph.D. degree in electrical and electronic engineering from Imperial College, London, U.K., in 2017.

Since 2017, he has been a Postdoctoral Researcher with the QUANTIC Group, Mines Paristech (Universit Paris Sciences and Lettres) and The National Institute for Research in Computer Science and Automation (INRIA) Paris, France. His main research interests include the stability of nonlinear dynamical systems, with an emphasis in the analysis of multistability, and model reduction of open quantum systems.

Corinne Doppmann received the B.Sc. and M.Sc. degrees in microengineering from the École Polytechnique Fédérale de Lausanne, Lausanne, Switzerland, in 2012 and 2014, respectively.

In 2014, she was an intern student working on her master's thesis on exoskeleton robots with the Computational Neuroscience Laboratories, Advanced Telecommunications Research Institute International, Kyoto, Japan.

Emre Sariyildiz (S'11–M'16) received the first Ph.D. degree in integrated design engineering from Keio University, Tokyo, Japan, in 2014, and second Ph.D. degree in control and automation engineering from Istanbul Technical University, Istanbul, Turkey, in 2016.

He was a Research Fellow with the Department of Biomedical Engineering and Singapore Institute for Neurotechnology, National University of Singapore, Singapore, from 2014 to 2017. Since 2017, he has been a Lecturer with the School of Mechanical, Materials, Mechatronic and Biomedical Engineering, University of Wollongong, NSW, Australia. His main research interests include control theory, robotics, mechatronics, and motion control.

Jun Morimoto (M'08) received the Ph.D. degree in information science from the Nara Institute of Science and Technology, Nara, Japan, in 2001.

He is the Head of the Department of Brain-Robot Interface, ATR Computational Neuroscience Laboratories. He was a Postdoctoral Fellow with Robotics Institute, Carnegie Mellon University, Pittsburgh, PA, USA. He joined ATR in 2002. He was also a member and a Group Leader of International Collaborative Research Project (ICORP) Computational Brain Project, Japan Science and Technology (JST) from 2004 to 2009.